SCIENCE CHINA
Technological Sciences

February 2012 Vol.55 No.2: 568–580
doi: 10.1007/s11431-011-4643-2

Coupling of wave and current numerical model with unstructured quadtree grid for nearshore coastal waters

ZHANG MingLiang[1*], WU WeiMing[2], LIN LiHua[3] & YU JiangNan[1]

[1] *School of Ocean Technology and Environment, Dalian Ocean University, Dalian 116023, China;*
[2] *National Center for Computational Hydroscience and Engineering, The University of Mississippi, University 38677, MS, USA;*
[3] *US Army Engineer Research and Development Center, 39180, MS, USA*

Received May 23, 2011; accepted October 12, 2011;

This paper presents 2D wave-current interaction model for evaluating nearly horizontal wave-induced currents in the surf-zone and coastal waters. The hydrodynamic model is the two-dimensional depth-averaged nonlinear shallow water equations by using an unstructured non-staggered and multiple-level quadtree rectangular mesh, this mesh information is stored in simple data structures and it is easy to obtain a locally high resolution for important region. The intercell fluxes are computed based on the HLL (Harten-Lax-van Leer) approximate Riemann solver with shock capturing capability for computing the dry-to-wet interface of coastal line. The effects of pressure and gravity are included in source term in the model, this treatment can simplify the computation and eliminate numerical imbalance between source and flux terms. The wave model readily provides the radiation stresses that represent the shortwave-averaged forces in a water column for the hydrodynamic model and the wave model takes into account the effect of wave-induced nearshore currents and water level. The coupling model is applied to verify different experimental cases and real life case of considering the wave-current interaction. The calculated results agree with analytical solution, experimental and field data. The results show that the modeling approach presented herein should be useful in simulating the nearshore processes in complicated natural coastal domains.

wave-current interaction, unstructured quadtree grid, finite volume method, HLL approximate Riemann solver, wave action spectral model

Citation: Zhang M L, Wu W M, Lin L H, et al. Coupling of wave and current numerical model with unstructured quadtree grid for nearshore coastal waters. Sci China Tech Sci, 2012, 55: 568–580, doi: 10.1007/s11431-011-4643-2

1 Introduction

Reliable prediction of wave motion in coastal areas is crucial to coastal engineering applications associated with nearshore morphologic change and harbor/inlet maintenance. In some areas, however, ambient tidal and other currents can be strong and their effect on wave transformation can be substantial. On entering shallow coastal waters, waves are modified by shoaling, refraction, diffraction and wave-current interaction before the wave energy dissipates [1, 2]. Radiation stresses from the excess momentum flux of the waves produce mean water level changes (setting up and setting down) and longshore or cross-shore currents. These wave-induced currents and water level setups play a major role in sediment and contaminant transport, pollutant mixing, etc. in the nearshore region. Very often the flow pattern consists of the combined interaction of tidal currents and a wave-induced current field. The complexity is further enhanced by the influence of the flow field on wave propagation. In order to protect as well as develop these coastal areas, knowledge of wave-current interactions and wave-induced bottom shear stress is thus necessary to understand

---

*Corresponding author (email: zhmliang_mail@126.com)

Report Documentation Page

Form Approved
OMB No. 0704-0188

1. REPORT DATE
28 DEC 2011

2. REPORT TYPE

3. DATES COVERED
00-00-2011 to 00-00-2011

4. TITLE AND SUBTITLE
Coupling of wave and current numerical model with unstructured quadtree grid for nearshore coastal waters

5a. CONTRACT NUMBER

5b. GRANT NUMBER

5c. PROGRAM ELEMENT NUMBER

6. AUTHOR(S)

5d. PROJECT NUMBER

5e. TASK NUMBER

5f. WORK UNIT NUMBER

7. PERFORMING ORGANIZATION NAME(S) AND ADDRESS(ES)
U.S. Army Engineer Research and Development Center,Coastal and Hydraulics Laboratory,3909 Halls Ferry Road,Vicksburg,MS,39180

8. PERFORMING ORGANIZATION REPORT NUMBER

9. SPONSORING/MONITORING AGENCY NAME(S) AND ADDRESS(ES)

10. SPONSOR/MONITOR'S ACRONYM(S)

11. SPONSOR/MONITOR'S REPORT NUMBER(S)

12. DISTRIBUTION/AVAILABILITY STATEMENT
Approved for public release; distribution unlimited

13. SUPPLEMENTARY NOTES

14. ABSTRACT

15. SUBJECT TERMS

16. SECURITY CLASSIFICATION OF:

a. REPORT	b. ABSTRACT	c. THIS PAGE	17. LIMITATION OF ABSTRACT	18. NUMBER OF PAGES	19a. NAME OF RESPONSIBLE PERSON
unclassified	**unclassified**	**unclassified**	**Same as Report (SAR)**	**13**	

Standard Form 298 (Rev. 8-98)
Prescribed by ANSI Std Z39-18

sediment dynamics, pollutant mixing and transport and bottom properties.

In order to solve the two-dimensional shallow water equations, a recent trend is the use of finite volume method (FVM) [3–9]. This is due to the simplicity of implementation, combined with good flexibility for space discretization. On the other hand, FVM can be interpreted as a finite-difference method applied to the conservative form of the mechanical balances in arbitrary coordinates and requires less computational effort than a finite element method [10, 11]. To obtain an accurate resolution of discontinuities of the flow motion, some different schemes have been developed by researchers. Because dam-break flows and storm wave flooding are usually in the mixed flow regimes and with discontinuities, the often used numerical schemes are the shock-capturing schemes, such as approximate Riemann solvers and TVD (Total Variation Diminishing) schemes. Recently, significant progress in the simulation of flood wave propagation due to a dam-break event was achieved by introducing the TVD schemes [12–14] and approximate Riemann solvers [15, 16]. Many of these methods have been verified and successfully applied to the simulation of dam-break flow over the fixed beds and estuary tidal flows by two-dimensional models [8, 9, 17, 18]. Because supercritical flows can be seen due to storm waves and surge tides through breached barrier islands or coastal inlets, hydrodynamic models should be capable of simulating multiple flow regimes such as subcritical, transcritical, or supercritical flows. The wave-induced nearshore currents in a coast make flow pattern more complex. An exclusive wave model is necessary to couple with the shallow water flow model in order to simulate both the wave field and the wave-induced flow field. Most two-dimensional depth-averaged models of wave-current interaction are based on the fixed rectangular grids or uniform curvilinear boundary-fitted grids and therefore simulate the large-scale flow features on a structured grid system [19–22], but it is not very efficient computationally for the grid to be of uniformly high resolution throughout the entire numerical domain. Quadtree grids have gained increasing popularity in recent years due to many of their obvious advantages: they are cheap and automatic to generate, mesh information is stored in simple data structures and it is easy to obtain a locally high resolution. Some coupling wave-current models with quadtree grid have been developed for evaluating nearly horizontal wave-induced currents in the surf-zone [23, 24].

In the present study, an explicit 2D shallow water hydrodynamic model is developed based on a finite volume method with quadtree mesh. In order to simulate wave field and wave-induced flow field in a coast area, the hydrodynamic model is combined with a steady state wave transformation and deformation model (CMS-Wave). The systematic integration of the wave model with the hydrodynamic model helps to develop a shock-capturing coastal flow model that can simulate wave transformations and deformations together with complex flow scenarios. The proposed model is applicable to both wet- and dry-bed and extensively by predicting dam-break flows and wave-current interactions for coastal area with natural topography. The results will be presented in the next sections.

2 Physical model

2.1 Wave model

The wave model is a two-dimensional spectral wave action model [25]. The model formulation is based on the parabolic approximation equation including diffraction terms and energy dissipation due to wave breaking and bottom friction. The model simulates steady state spectral transformation of directional random waves and waves can propagate from the seaward boundary toward shore and vice versa. The wave model takes into account the effect of wave breaking, shoaling, refraction, diffraction, wave-current interaction, bottom friction and the wave-action balance equation is as follows:

$$\begin{aligned}&\frac{\partial\left(C_x N\right)}{\partial x}+\frac{\partial\left(C_y N\right)}{\partial y}+\frac{\partial\left(C_\theta N\right)}{\partial \theta}\\&=\frac{\kappa}{2\sigma}\left[\frac{\partial}{\partial y}\left(CC_{\mathrm{g}}\cos^2\theta\frac{\partial N}{\partial y}\right)-\frac{CC_{\mathrm{g}}}{2}\cos^2\theta\frac{\partial^2 N}{\partial y^2}\right]\\&\quad-\varepsilon_{\mathrm{b}}N-Sou,\end{aligned}\tag{1}$$

where x, y are the horizontal coordinates in two directions; $N=E(\sigma, \theta)/\sigma$ is the wave-action density to be solved and is a function of frequency σ and direction θ, which is defined as angle of wave relative to the x-axis. The spectral wave density $E(\sigma, \theta)$ represents the wave energy per unit water surface area per frequency interval in eq. (1). The first term on the right-hand side of eq. (1) represents wave diffraction as formulated from the parabolic wave approximation assumption. A default value of $\kappa=2.5$ is used for the diffraction intensity parameter suggested by Mase in the present study [25]. C and C_{g} are the wave celerity and group velocity, respectively, and ε_{b} is parameterization of wave breaking energy dissipation. *Sou* is the source terms (e.g., wind forcing, bottom friction loss, nonlinear wave-wave interaction term etc.) [26]. These characteristic wave velocities with respect to x, y and θ coordinates are accordingly C_x, C_y and C_θ defined as

$$C_x=C_{\mathrm{g}}\cos\theta+u,C_y=C_{\mathrm{g}}\cos\theta+v,\tag{2}$$

$$\begin{aligned}C_\theta=&\frac{\sigma}{\sin 2kh}\left(\sin\theta\frac{\partial h}{\partial x}-\cos\theta\frac{\partial h}{\partial y}\right)+\cos\theta\sin\theta\frac{\partial u}{\partial x}\\&-\cos^2\theta\frac{\partial u}{\partial y}+\sin^2\theta\frac{\partial v}{\partial x}-\sin\theta\cos\theta\frac{\partial v}{\partial y},\end{aligned}\tag{3}$$

where u and v are current velocity components in the x and y directions, respectively, k is the wave number, and h is water depth. Eq. (1) is solved for wave-action density N by a forward-marching first-order upwind finite-difference method with rectangle grid, the detailed description of solution methodology can be found in ref. [25]. The importance of this function is examined for four wave breaking formulas, in this study, the extended Miche formula is used for calculating wave breaking term, a summary description of the parameterized wave breaking formulas is presented by Zheng et al. [27].

2.2 Wave-induced nearshore current equation

The numerical model used consists of the two-dimensional shallow water equations describing the conservation of mass and momentum. The shallow water equation written in conservation and vector form are

$$\frac{\partial U}{\partial t}+\frac{\partial E}{\partial x}+\frac{\partial G}{\partial y}=\frac{\partial E_d}{\partial x}+\frac{\partial G_d}{\partial y}+S. \tag{4}$$

In which, U is the vectors of conserved variables, $E(U)$, $G(U)$, $E_{\mathrm{d}}(U)$ and $G_{\mathrm{d}}(U)$ in eq. (4) are convection fluxes and diffusion fluxes in the x and y directions, respectively, $S(U)$ is source terms which can be defined respectively as follows:

$$U=\begin{bmatrix} h \\ hu \\ hv \end{bmatrix},\ E=\begin{bmatrix} hu \\ huu \\ huv \end{bmatrix},\ G=\begin{bmatrix} hv \\ huv \\ hvv \end{bmatrix},\ E_{\mathrm{d}}=\begin{bmatrix} 0 \\ \nu_t\dfrac{\partial uh}{\partial x} \\ \nu_t\dfrac{\partial vh}{\partial x} \end{bmatrix},$$
$$G_{\mathrm{d}}=\begin{bmatrix} 0 \\ \nu_t\dfrac{\partial uh}{\partial y} \\ \nu_t\dfrac{\partial vh}{\partial y} \end{bmatrix},\ S=\begin{bmatrix} 0 \\ gh\dfrac{\partial z}{\partial x}-S_{\mathrm{b}x}-\tau_{Sx}-\tau_{\mathrm{w}x}+f_{\mathrm{c}}hv \\ gh\dfrac{\partial z}{\partial y}-S_{\mathrm{b}y}-\tau_{Sy}-\tau_{\mathrm{w}y}-f_{\mathrm{c}}hu \end{bmatrix} \tag{5}$$

where g is the acceleration due to gravity, $S_{\mathrm{b}x}$ and $S_{\mathrm{b}y}$ are bed shear stress terms with x and y components defined by the velocities, Z is water level, z_{b}, the bed surface elevation above a reference datum. The unit-widths hu and hv are the conservative dependent variables, grouped in the column vector U. τ_{sx} and τ_{sy} are wave force terms with x and y components; f_{c} is the Coriolis parameter. $\tau_{\mathrm{w}x}$ and $\tau_{\mathrm{w}y}$ are the surface wind stresses, respectively.

In the depth-averaged parabolic model the eddy viscosity is given for pure current:

$$\nu_t=\alpha u_* h. \tag{6}$$

In which u_* is the bed shear velocity $u_*=[c_f(u^2+v^2)]^{1/2}$ and α is an empirical coefficient between 0.3–1.0. The transition between surf-zone mixing and oceanic mixing seaward of the breakpoint is represented in CMS-M2D [20] by a weighted mixing coefficient specified as

$$\nu_t=(1-D)\alpha u_* h+D\Lambda u_m H, \tag{7}$$

where Λ is the mixing parameter equal to 1.0, u_m is the amplitude of the horizontal component of the wave orbital velocity at the bottom given by

$$u_m=\frac{gHT}{\left[2\lambda\cosh\left(\dfrac{2\pi(h+\eta)}{\lambda}\right)\right]}, \tag{8}$$

where H is wave height, T is wave period, η is deviation of the water-surface elevation from the still-water level, λ is the coefficient for u_m which can be seen in ref. [20], $D=H/(h+\eta)$.

$S_{\mathrm{b}x}$ and $S_{\mathrm{b}y}$ are bed shear stress terms with x and y components defined by the velocities for the situation without waves,

$$S_{\mathrm{b}x}=gn^2u\sqrt{u^2+v^2}\,h^{-1/3};\ S_{\mathrm{b}y}=gn^2v\sqrt{u^2+v^2}\,h^{-1/3}, \tag{9}$$

where n is the manning's roughness coefficient. In the case of simulating wave-induced currents, the near bed orbital velocity has to be taken into account here. Nishimura's approximation is used to calculate the shortwave-averaged bottom stresses under combined currents and waves in this study [28]:

$$\begin{aligned} S_{\mathrm{b}x}&=n^2h^{-3/4}\left\{\left(U_{\mathrm{w}c}+\frac{\omega_b^2}{U_{wc}}\cos^2\gamma\right)u+\left(\frac{\omega_{\mathrm{b}}^2}{U_{wc}}\cos\gamma\sin\gamma\right)v\right\},\\ S_{\mathrm{b}y}&=n^2h^{-3/4}\left\{\left(\frac{\omega_{\mathrm{b}}^2}{U_{\mathrm{w}c}}\cos\gamma\sin\gamma\right)u+\left(U_{\mathrm{w}c}+\frac{\omega_{\mathrm{b}}^2}{U_{\mathrm{w}c}}\cos^2\gamma\right)v\right\}, \end{aligned} \tag{10}$$

$$\omega_{\mathrm{b}}=\frac{\sigma H_s}{\pi\sinh(kH)}. \tag{11}$$

In which γ is wave angle relative to the x-axis, H_{s} is significant wave height. $U_{\mathrm{w}c}$ is the resultant velocity from the shortwave-averaged and the wave-orbital velocities given by

$$\begin{aligned} U_{\mathrm{w}c}=&\frac{1}{2}\sqrt{\left|u^2+v^2+\omega_{\mathrm{b}}^2+2\left(u\cos\gamma+v\sin\gamma\right)\omega_{\mathrm{b}}\right|}\\ &+\frac{1}{2}\sqrt{\left|u^2+v^2+\omega_{\mathrm{b}}^2-2\left(u\cos\gamma+v\sin\gamma\right)\omega_{\mathrm{b}}\right|}. \end{aligned} \tag{12}$$

The wave force is calculated by using the following equations:

$$\tau_{Sx}=-\frac{1}{\rho}\left(\frac{\partial S_{xx}}{\partial x}+\frac{\partial S_{xy}}{\partial y}\right), \tag{13}$$

$$\tau_{Sy}=-\frac{1}{\rho}\left(\frac{\partial S_{xy}}{\partial x}+\frac{\partial S_{yy}}{\partial y}\right), \tag{14}$$

where S_{xx}, S_{xy}, and S_{yy} are wave-driven radiation stresses.

Radiation-stress tensor calculations are based on linear wave theory. They represent the summation of standard tensor formulations across the defined spectrum. For a coordinate system with the x-axis oriented normal to the shoreline, the tensor components are as follows [20]:

$$S_{xx} = \iint \frac{E(\sigma,\theta)}{2}\left[0.5\left(1+\frac{2k(h+\eta)}{\sinh 2k(h+\eta)}\right)\left(\cos^2 2\theta+1\right)-0.5\right]\mathrm{d}\sigma\mathrm{d}\theta, \tag{15}$$

$$S_{xy} = \iint \frac{E(\sigma,\theta)}{2}\left[0.5\left(1+\frac{2k(h+\eta)}{\sinh 2k(h+\eta)}\right)\sin 2\theta\right]\mathrm{d}\sigma\mathrm{d}\theta, \tag{16}$$

$$S_{yy} = \iint E(\sigma,\theta)\left[0.5\left(1+\frac{2k(h+\eta)}{\sinh 2k(h+\eta)}\right)\left(\sin^2 2\theta+1\right)-0.5\right]\mathrm{d}\sigma\mathrm{d}\theta. \tag{17}$$

The Coriolis parameter is given as

$$f_{\mathrm{c}} = 2\Omega\sin(\varphi), \tag{18}$$

where Ω is the angular frequency of the Earth's rotation, and ϕ is latitude.

Surface wind stresses are given by the following empirical wind shear stress formulations:

$$\tau_{\mathrm{w}x} = c_{\mathrm{d}}\frac{\rho_{\mathrm{a}}}{\rho_{\mathrm{w}}}W^2\sin(\beta), \tag{19}$$

$$\tau_{\mathrm{w}y} = c_{\mathrm{d}}\frac{\rho_{\mathrm{a}}}{\rho_{\mathrm{w}}}W^2\cos(\beta), \tag{20}$$

where C_{d} is the wind drag coefficient; ρ_{a} and ρ_{w} are density of air and water; W is wind speed measured at 10 m above the sea level; and β is the angle of wind direction relative to x-axis.

3 Grid type and numerical discretization

3.1 Quadtree grid and data structure

Because of the complexity of computational domain, a simple structured rectangular mesh requires a large number of cells to resolve the detailed flow pattern near the dam breaking location, navigation channels and in-stream structures. To optimize the use of computational resources, we use the multiple-level quadtree rectangular mesh with local refinement. In this mesh, various levels of fine cells are placed close to the dam-break locations and in-stream structures or inlet areas where the flow gradients are high, while coarse grids are used in the low-gradient regions. To simplify the mesh, a cell is refined by splitting into four equal child cells. Corresponding to this refining, any cell has one or two faces on each of its north, south, west, and east sides, as shown in Figures 1 and 2, so that the computational mesh will be less complicated [29].

The data structure for the quadtree mesh can be managed in several ways: block-structured, hierarchical tree, and fully unstructured. The block-structured approach divides the domain into multiple blocks, each of which is treated as structured. Interfaces between blocks need to be specially handled to ensure mass and momentum balance through them. The tree data structure uses parent and child relations and requires tree traverse to determine the mesh connectivity. In the fully unstructured approach, all the cells are numbered in a one-dimensional sequence, and pointers are used to determine the connectivity of neighboring cells for each cell. Among the three approaches, the fully unstructured approach is simpler and thus is used in this study. As mentioned in Section 1, another issue in simulation of incompressible flow is the location of primary variables: velocity and water level. On the non-staggered grid, all the primary variables are located at the center of cells. The computer code based on non-staggered grid is simpler and requires less memory, and the non-staggered grid is simpler in handling the interface between coarse and fine cells.

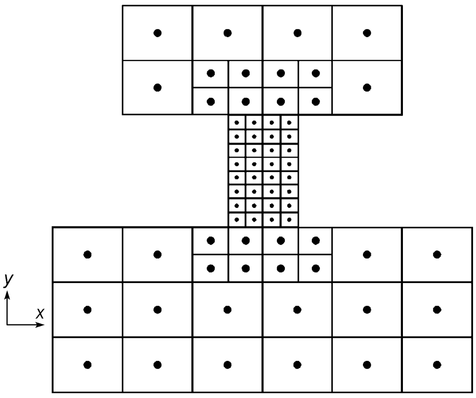

Figure 1 Example of quadtree mesh system.

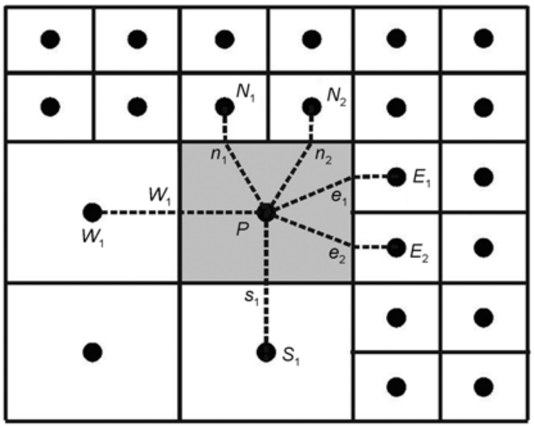

Figure 2 Control volume in a quadtree mesh based on non-staggered grid.

3.2 Finite volume method

The numerical representation of physical domain is obtained by using an unstructured mesh, composed of quadtree elements. Each of them must be considered as an elementary control volume. Eq. (4) can be integrated over a control volume V as

$$\int_V \frac{\partial U}{\partial t}+\int_V \frac{\partial E}{\partial x}\mathrm{d}V+\int_V \frac{\partial G}{\partial y}\mathrm{d}V=\int_V \frac{\partial E_d}{\partial x}\mathrm{d}V +\int_V \frac{\partial G_d}{\partial y}\mathrm{d}V+\int_V S\mathrm{d}V. \quad (21)$$

Applying the Gauss theorem to eq. (21), discretizing eq. (21) over a time interval by using the explicit scheme in time, one can obtain:

$$\begin{aligned}(U)_P^{n+1} &= (U)_P^n-\Delta t\left(\sum_k E_{ek}\Delta y_{ek}-\sum_k E_{wk}\Delta y_{wk}\right)\\ &-\Delta t\left(\sum_k G_{nk}\Delta x_{nk}-\sum_k G_{sk}\Delta x_{sk}\right)\\ &+\Delta t\left(\sum_k G_{dnk}\Delta x_{nk}-\sum_k G_{dsk}\Delta x_{sk}\right)\\ &+\Delta t\left(\sum_k E_{dek}\Delta y_{ek}-\sum_k E_{dwk}\Delta y_{wk}\right)+\Delta t\left(S_u\right)_P. \quad (22)\end{aligned}$$

The detailed definition about notations (e, w, n and s) can be found in Figure 2, the interpolation for water level (velocity etc.) at between cell (node P) and a child cell (node $E1$) can be expressed in eqs. (23) and (24):

$$fin=\frac{\sqrt{\Delta x_P{}^2+\Delta y_{E_1}^2}}{\Delta x_{E_1}+\sqrt{\Delta x_p^2+\Delta y_{E_1}^2}}, \quad (23)$$

$$z_{e_1}=fin*z_{E_1}+(1-fin)*z_P. \quad (24)$$

3.3 HLL scheme

A detailed description of the HLL (Harten-Lax-van Leer) scheme can be found in Toro [17] and Ying [8] including a complete discussion regarding the Riemann problem and the reasons for a special treatment of the cells located on the wave front or shore line (wet/dry boundary). The HLL scheme assumes and defines the flux at an interface as

$$F_{\mathrm{HLL}}=\begin{cases}F_{\mathrm{L}} & \text{if } S_{\mathrm{L}}\geqslant 0,\\ F^* & \text{if } S_{\mathrm{L}}\leqslant 0\leqslant S_R,\\ F_{\mathrm{R}} & \text{if } S_{\mathrm{R}}\leqslant 0.\end{cases} \quad (25)$$

In which F_{L} and F_{R} are the flux evaluated at the left-hand and the right-hand sides of each cell interface. $\boldsymbol{F}^*$ denotes the flux at the intermediate state, given by

$$F^*=\frac{S_{\mathrm{R}}F_{\mathrm{L}}-S_{\mathrm{L}}F_{\mathrm{R}}+S_{\mathrm{L}}S_{\mathrm{R}}\left(U_{\mathrm{R}}-U_{\mathrm{L}}\right)}{S_{\mathrm{R}}-S_{\mathrm{L}}}. \quad (26)$$

In which U_{L} and U_{R} are the conservative variable vectors evaluated on the left-hand and the right-hand sides of each cell. The symbols S_{L} and S_{R} represent the celerity of the waves, separating constant states of the local Riemann problem solution at cell interfaces, they can be estimated as follows:

$$S_{\mathrm{L}}=\min\left(u_{\mathrm{L}}-\sqrt{gh_{\mathrm{L}}},u^*-\sqrt{gh^*}\right), \quad (27)$$

$$S_{\mathrm{R}}=\min\left(u_{\mathrm{R}}+\sqrt{gh_{\mathrm{R}}},u^*+\sqrt{gh^*}\right), \quad (28)$$

$$u^*=\frac{1}{2}\left(u_{\mathrm{L}}+u_{\mathrm{R}}\right)+\sqrt{gh_{\mathrm{L}}}-\sqrt{gh_{\mathrm{R}}}, \quad (29)$$

$$\sqrt{gh^*}=\frac{1}{2}\left(\sqrt{gh_{\mathrm{L}}}+\sqrt{gh_{\mathrm{R}}}\right)+\frac{1}{4}\left(u_{\mathrm{L}}-u_{\mathrm{R}}\right). \quad (30)$$

The symbols h_{L} and h_{R} are the water depth of the left and right states. Note that for a dry bed problem, the wave speeds S_{L} and S_{R} can be estimated according to the following expressions:

$$S_{\mathrm{L}}=u_{\mathrm{L}}-\sqrt{gh_{\mathrm{L}}},\ S_{\mathrm{R}}=u_{\mathrm{L}}+2\sqrt{gh_{\mathrm{L}}} \quad \text{for right dry}, \quad (31)$$

$$S_{\mathrm{L}}=u_{\mathrm{R}}-2\sqrt{gh_{\mathrm{R}}},\ S_{\mathrm{R}}=u_{\mathrm{R}}+\sqrt{gh_{\mathrm{R}}} \quad \text{for left dry bed}. \quad (32)$$

3.4 Stability analysis

A variable Δt, adapted to hydraulic parameters variability, is used. It is well known that computation stability for explicit scheme model requires a Courant-Friedrichs-Lewy (CFL) number less than 1. This parameter in the FVM context defined as

$$CFL=\mathrm{Max}\left\{\frac{\Delta t}{\Delta x}\left(|u|+\sqrt{gh}\right),\frac{\Delta t}{\Delta y}\left(|v|+\sqrt{gh}\right)\right\}\leqslant 1. \quad (33)$$

The time step can be either automatically selected by the program based on the consideration of the CFL condition or directly specified by the user.

4 Model validation and verification

4.1 Dam break on dry and wet beds

The aim of this test case is to study the ability of the model to simulate discontinuous flow and the front wave propagation over dry and wet beds. Considering a horizontal and frictionless channel of 1200 m long and 1 m wide, a column of water is separated by a dam located at x=500 m. This test case is simulated for both wet and dry bed situations, the initial upstream water depth is 10 m. The downstream water depth is 5 m for wet bed and 0 m for dry bed, the tolerance depth for dry bed is set as 0.0001 m. The space discretization is set as Δx=1 m and time step is set as Δt= 0.1 s, at t=

0 the dam is removed instantaneously. The results are reported up to 30 s after the removal of the dam. Figures 3(a) and 3(b) compare the water depth and the velocity for the wet bed case and Figures 4(a) and 4(b) compare water depth and the velocity for the dry bed case. The computed water depth and velocities follow the exact solutions.

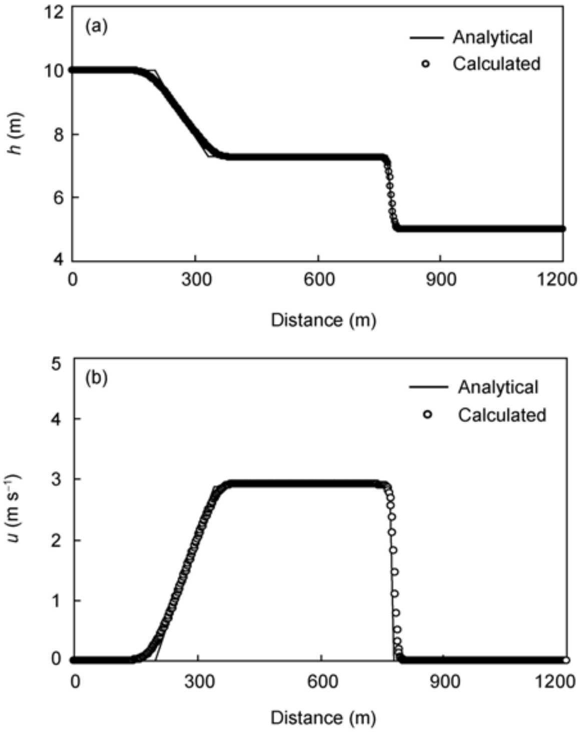

Figure 3 Dam break on wet bed. (a) Water depth; (b) velocity.

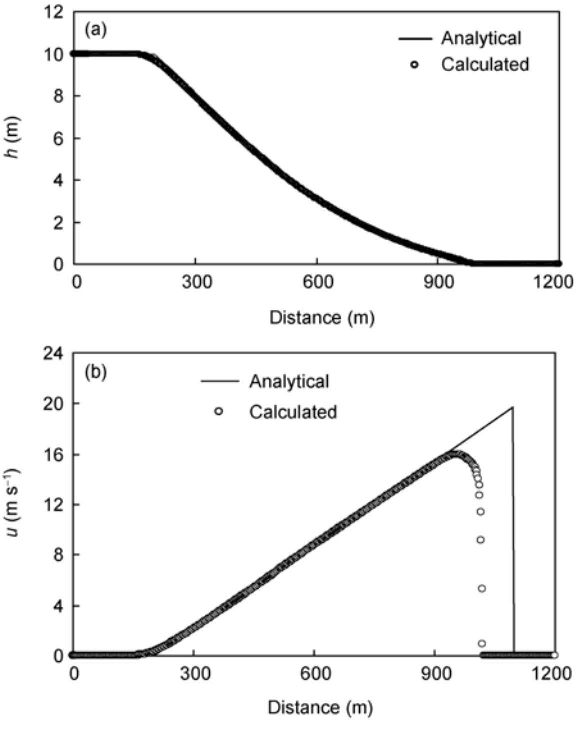

Figure 4 Dam break on dry bed. (a) Water depth; (b) velocity.

4.2 Flow over a triangular obstacle

This test is carried out to reproduce the laboratory dam-break flow over a triangular hump recommended by the EU CADAM project [15]. The physical experiment included complex hydraulic properties such as shocks, transitions between wet and dry beds and flow over an obstacle. The laboratory setup is illustrated in Figure 5. The experiment consists of a reservoir with water up to 0.75 m contained by a dam at x =15.5 m and a dry bed downstream within a rectangular channel of 20.5 m in length. A symmetric triangular obstacle (6 m long, 0.4 m high) is placed on the channel with its peak located at 13 m downstream of the dam. In order to observe depth evolutions gauge points are located at 4 m (G4), 10 m (G10), 11 m (G11), 13 m (G13) and 20 m (G20) from the dam as shown in Figure 5. The upstream boundary is wall and the downstream boundary is free flow. The Manning's roughness coefficient is set as 0.0125 s $m^{-1/3}$ with the same value of the experiment. In the computation, x=0.1 m, t =0.01 s and h=0.0001 m as dry bed are used and the simulation is carried out for 100 s. The water depth variations with respect to time at the five gauge points are shown in Figures 6(a)–6(e). It can be seen that the predicted water depth evolutions and arrival time of the wave are quite comparable with the measured data at every gauge point. The transition from wet to dry at the gauge point G13 is well predicted. The general trend is captured well at G20 (after the hump) and the water depth is slightly overestimated before 20 s, which is also predicted by other researchers by using different numerical schemes [14, 15]. Overall, the comparison between the numerical predictions and measurements is satisfactory, the wet-dry transitions are simulated with very high accuracy by the present model. This confirms the effectiveness of this method on flux and the effects of pressure and gravity in source term. All the results are computed by using the depth-averaged 2D model, the reason with slight discrepancies may be that the 2D models cannot accurately simulate the complex 3D flow phenomenon.

4.3 Wave-induced longshore current

Kuriyama and Ozaki [30] carried out field measurements of the longshore current at Hazaki Oceanographical Research Facility (HORF) located on the Japan Pacific coast. The HORF research pier is 427 m long, and the current measurements were made from the HORF pier by using a float.

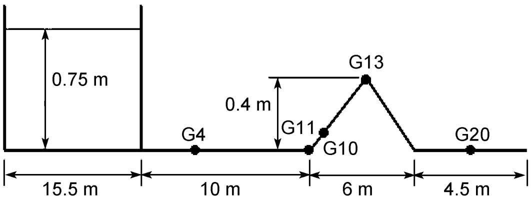

Figure 5 Geometry and gauge locations in the experiment.

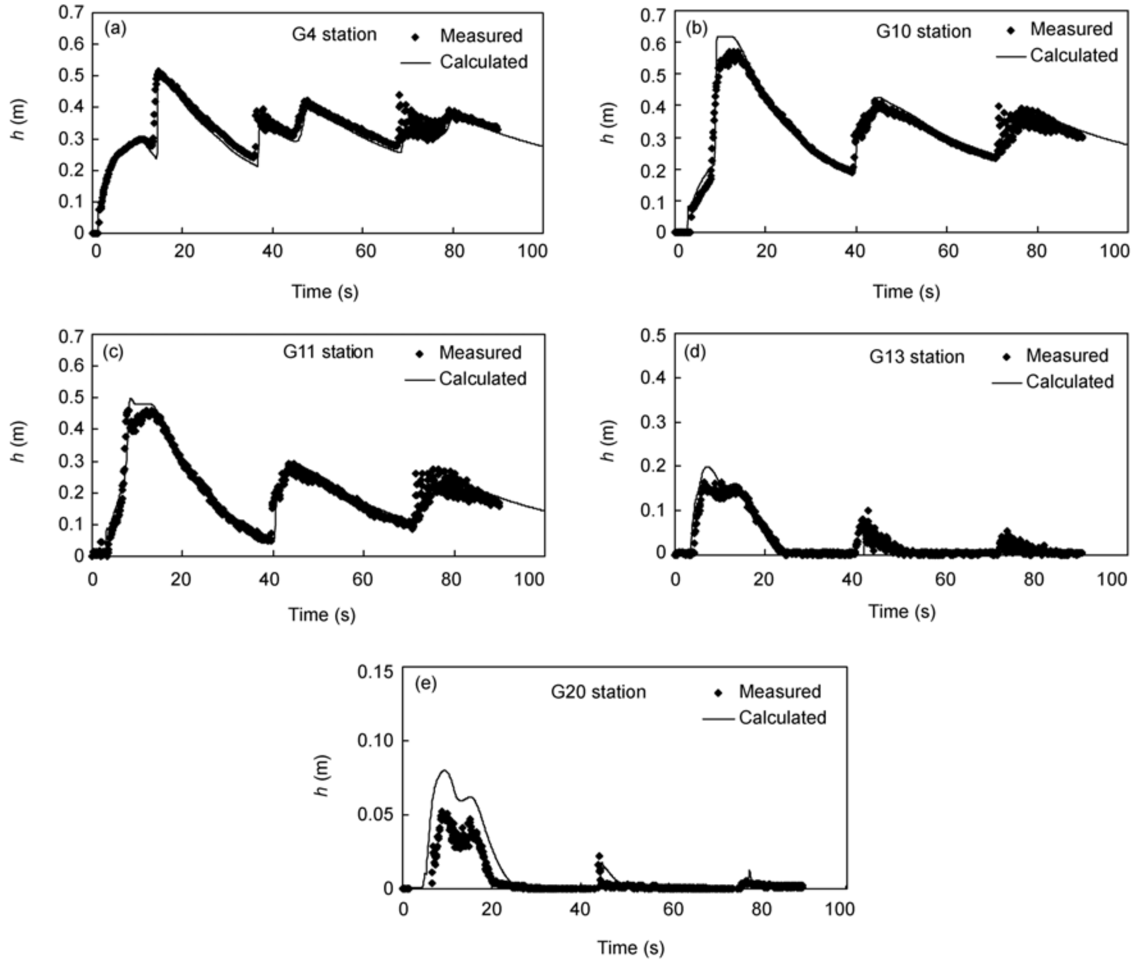

Figure 6 Computed and measured water depth variations at stations (a) G4; (b) G10; (c) G11; (d) G13; and (e) G20.

The beach at HORF, having a mean slope of 1/60, often includes several longshore bars, leading to complex wave transformation with shoaling, breaking, and reforming taking place as shown in Figure 7. The significant wave height is 2.6 m and significant wave period is 8.86 s, the wave direction angle α is 27° in this case study [1]. A time step of 0.2 s is used, the Manning's n is set as 0.015 and the simulation stops until steady state reaches. Figure 8 shows the calculated and measured distribution of the longshore current. Breaking on the seaward side of the bar yields two peaks in the longshore current distribution, which is in agreement with the measurements. The seaward-most peak agrees with the observed one, including the correct location, the shoreward-most peak has the correct magnitude, but is located somewhat shoreward of the measured peak. The mixing parameter is set to Λ=1.0 in this study. Figure 9 compares the calculated and measured significant wave height. Figure 10 shows the calculated longshore current pattern for Kuriyama and Ozaki field experiment [30]. The results demonstrate that the coupling model gives predictions in close agreement with experimental data, whereas numerical model somewhat overestimates the wave heights in the breaker region. As would be expected, the wave

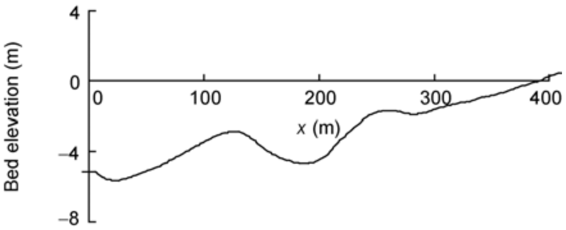

Figure 7 Bed profile for Kuriyama and Ozaki field experiment [30].

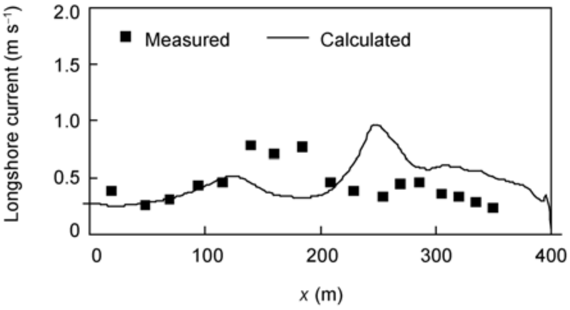

Figure 8 Calculated and measured longshore current for Kuriyama and Ozaki field experiment [30].

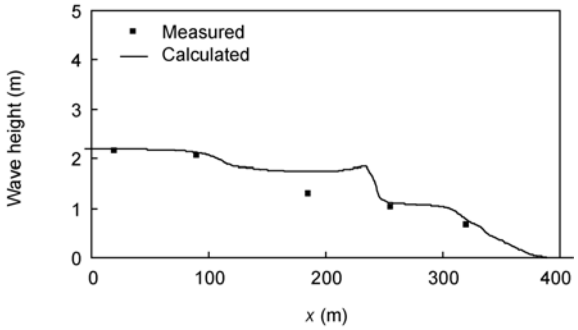

Figure 9 Calculated and measured wave height for Kuriyama and Ozaki field experiment [30].

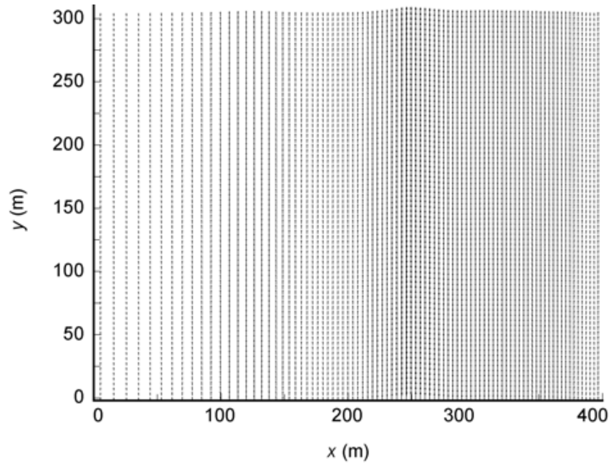

Figure 10 Calculated longshore current for Kuriyama and Ozaki field experiment [30].

heights rapidly decrease to zero onshore after breaking. This rapid loss in height of the broken waves may promote strong radiation stresses, which in turn may create large and possibly unstable currents.

5 Model applications

5.1 Tidal flow through an idealized inlet

The developed model is tested in a hypothetical case of tidal flow through an idealized inlet. The inlet is 150 m wide. Its east end is connected with a rectangular bay of about 1250 m × 2750 m in *x* and *y* directions, and its west end is open sea. The sea bed has a constant equilibrium cross-shore profile with a maximum still water depth of about 20 m, while the bay and the inlet have a flat bed that is 3 m below the still sea level. Two jetties are located on the sea side of the inlet. A four-level quadtree rectangular mesh (dots are cell centers) is used, as shown in Figure 11. The finest grid spacing near the inlet is 12.5 m by 12.5 m, while the coarsest grid spacing is 100 m by 100 m in the sea and 50 m by 50 m inside the bay. An M2 tide is specified at the sea and two cross-shore boundaries, the computational time step is 2 s. Figure 12 shows the simulated flow pattern during flood

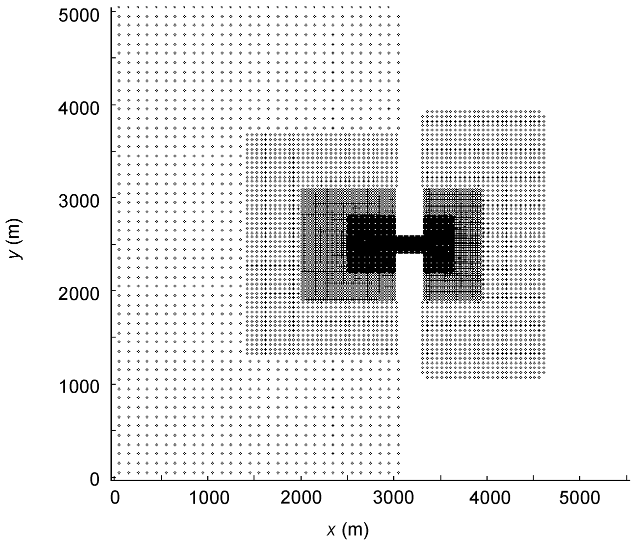

Figure 11 Mesh near an idealized inlet (dots are cell centers).

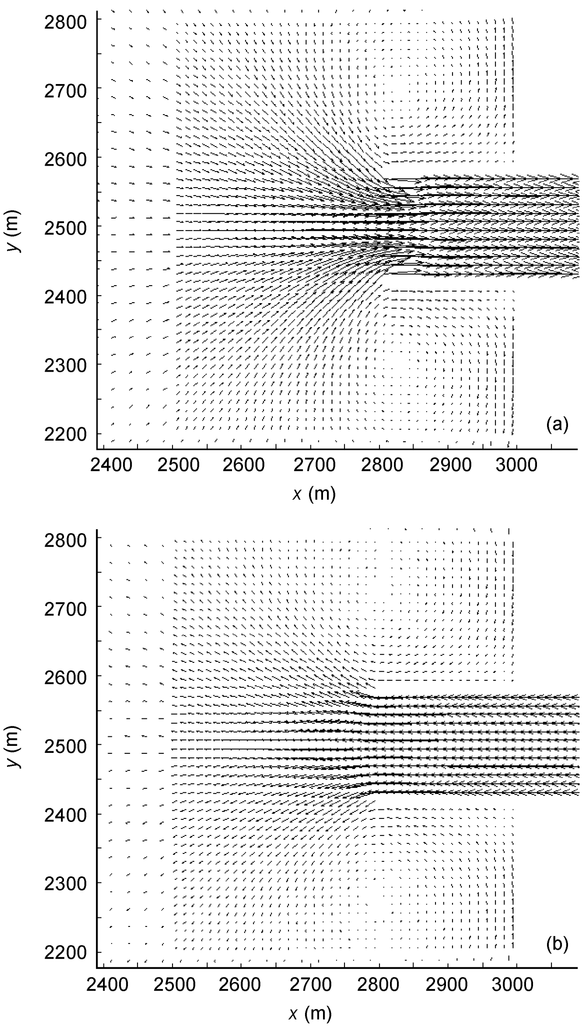

Figure 12 Simulated flow pattern in the bay during flood tide (a) and ebb tide (b).

and ebb tides. One can see that the flood jet eddies are simulated reasonably well. The recirculation flows cover four levels of the refined mesh, and the transition between flows on fine and coarse grids is very smooth, the flow patterns are symmetric about the centerline of the inlet and two symmetric vortexes can be found beside jetties. This test demonstrates that the numerical discretization and solution methods in the developed model are adequate to handle the unstructured quadtree mesh. Because there are no measurement data, the performance of the developed model is only qualitatively verified in this hypothetical case. Quantitative validation of the model in case of unsteady flow will be carried out in the next case.

5.2 Tidal flow in Gironde Estuary

The Gironde Estuary is located in southwestern France. It receives runoff from the Garonne River and the Dordogne River, and empties into the Atlantic Ocean, as shown in Figure 13. The water-surface width varies from 2 to 14 km, and the flow depth in the navigation channel is about 6–30 m. The estuary is partially mixed and macrotidal, with a 12 hour and 25 minutes tidal lunar period and a tidal amplitude of 1.5–5 m at the mouth [31]. The simulation domain is about 80 km long, starting from the mouth to the Garonne River and the Dordogne River. Because the domain is simple, a uniform mesh is used here, with a size of 250 m × 125 m for each cell. The measured data from May 19 to 25 of 1975 are used to validate the model. The computational time step is 5 s. At the estuary mouth, the tidal elevation is given according to the recorded time series at the station "Pointe de Grave". At the two upstream ends, the flow discharges of the Garonne River and the Dordogne River are specified according to the measured data at La Réole and Pessac. The Manning's n is set as 0.015. Figure 14 shows the comparison of the measured and simulated water levels at four selected stations. The amplitude and phase are well predicted by the present numerical model, no obvious phase difference exists between the measured and simulated tidal levels. Figure 15 shows the comparison of the measured and simulated flow velocities at five selected stations. The measured flow velocities are 1 m under the water surface and 1 m above the seabed, respectively. The simulated depth-averaged flow velocity stays between them, the agreement is reasonably good. The flow fields in flood and ebb tides are reasonably well predicted, as shown in Figure 16.

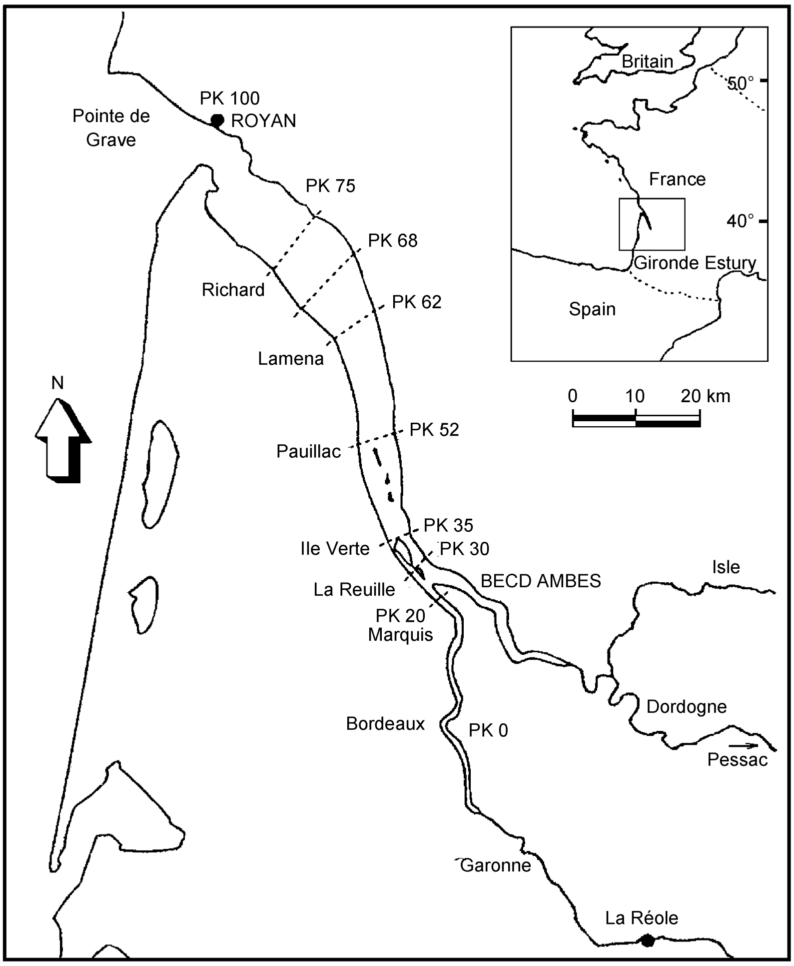

Figure 13 Sketch of Gironde Estuary, France.

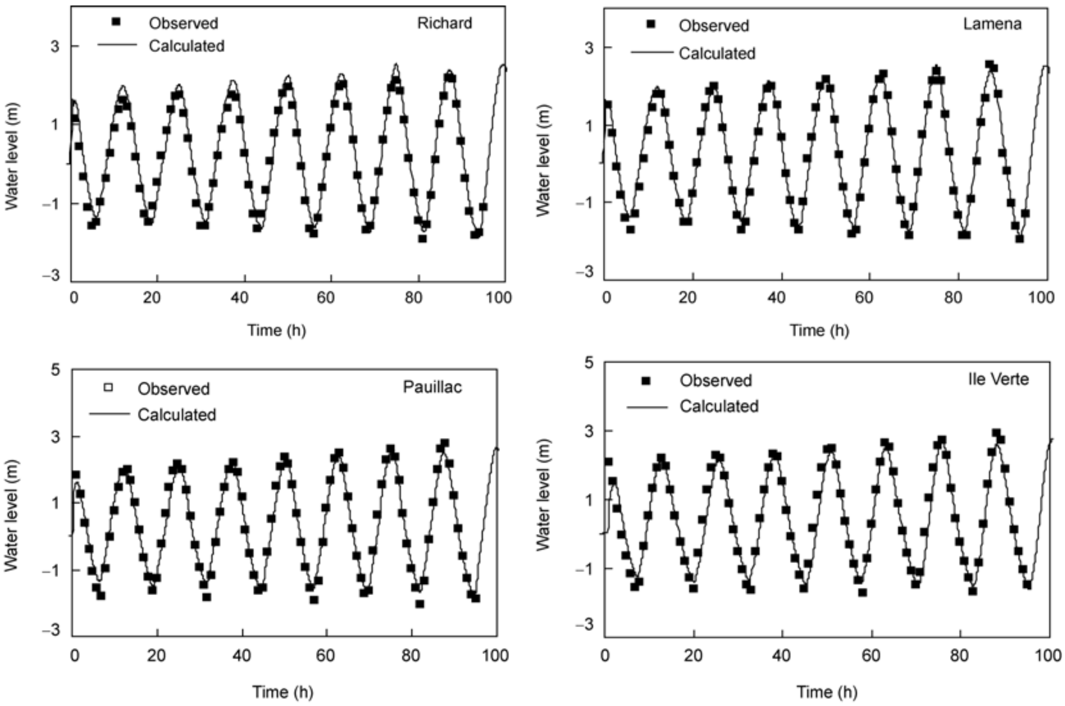

Figure 14 Computed and measured water surface level variations at different stations.

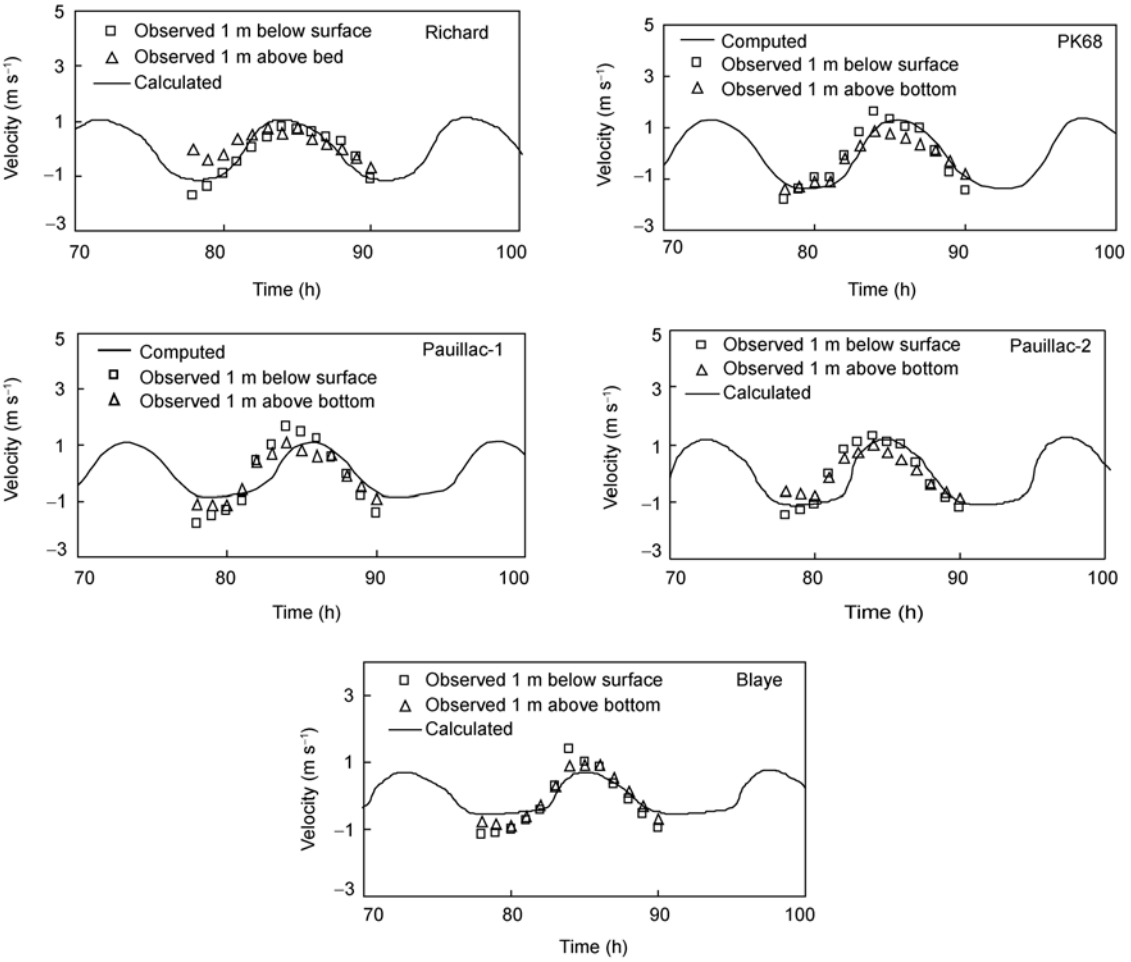

Figure 15 Computed and measured velocities at different stations.

5.3 Tidal flow in Grays Harbor

Grays Harbor is located on the southwest Washington coast about 72 km north of the Columbia River. The estuary is one of the largest in the continental United States. As part of the U. S. Army Corps of Engineers Grays Harbor Estuary Physical Dynamics Study, data of current and waves were measured during September to November of 1999 [1, 32]. The estuary has a wetted surface area of approximately 146 km^2 at mean higher high water and 45 km^2 at mean lower low water. The main input of fresh water is from the Chehalis River. The 5 km wide entrance has two convergent rock jetties that extend from spit points, as shown in Figure 17. The spectral waves from the NOAA buoy 46029 were input data at the model boundaries every 3 h. The mesh is refined around the jetties and near the channels, the finest grid spacing is 25 m near the jetties and the coarsest one is 800 m near the offshore boundary at deep water. The computational time step is 1 s. The measured water levels from the station nearest to the offshore boundary are used as the boundary condition. The wave radiation stresses calculated by the wave model are considered in the simulation of tidal current. Figure 18 compares the computed and measured water levels at Stations 1, 5 and tide 2, and Figure 19 compares the computed and measured current speeds at Stations 2 and 5 for a period of 8 days in the late September of 1999. Figure 20 compares the computed and measured current direction at Station 5 with good agreement and no obvious phase difference. Figure 21 compares the computed and measured wave heights at the selected stations. From these figures, one can see that the agreement between those calculated results and measured data is generally good. This model can also simulate the wetting and drying processes on the floodplain due to tide change. This demonstrates that the coupling model can handle the moving coastal line efficiently and reproduce the tidal water level and current speed reasonably well.

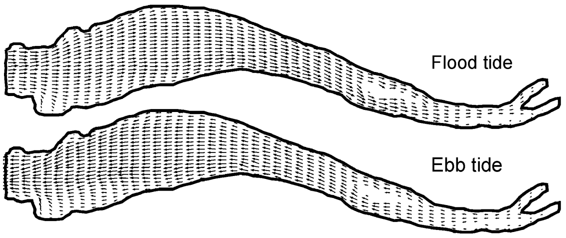

Figure 16 Simulated flow patterns in Gironde Estuary.

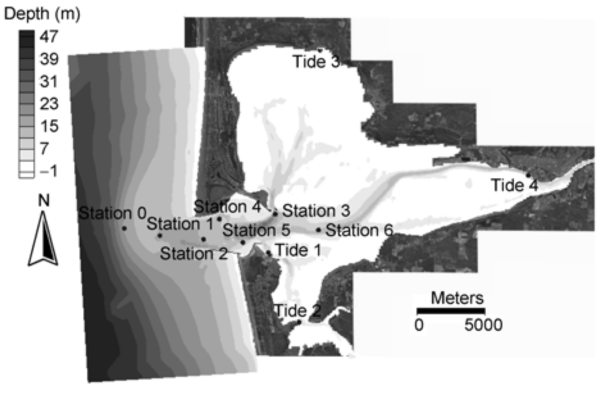

Figure 17 Topography and measurement stations at Grays Harbor.

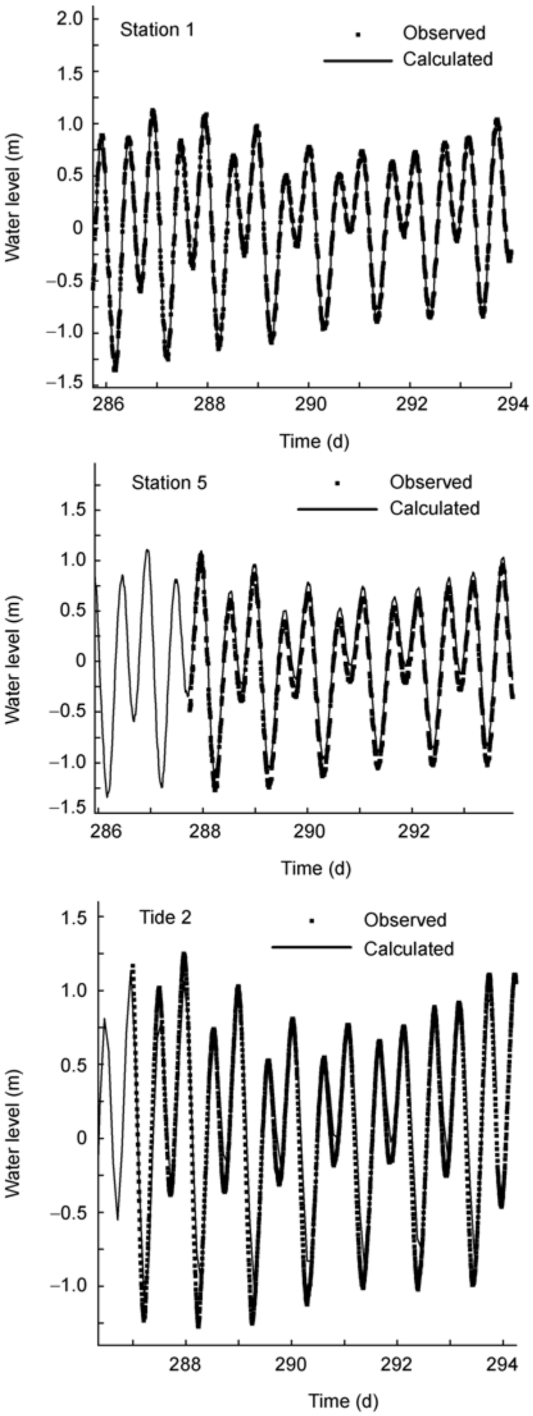

Figure 18 Measured and calculated tide levels at Grays Harbor.

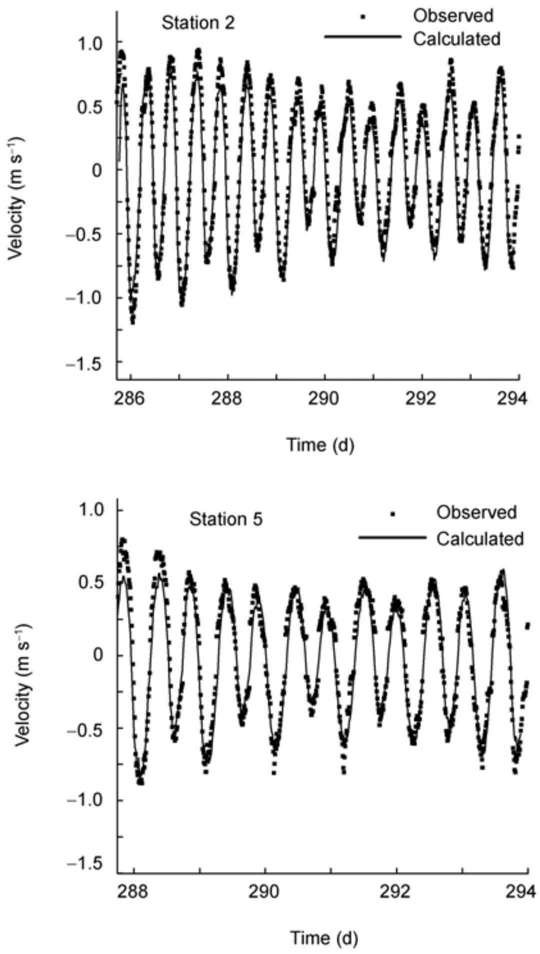

Figure 19 Measured and calculated current velocities at Grays Harbor.

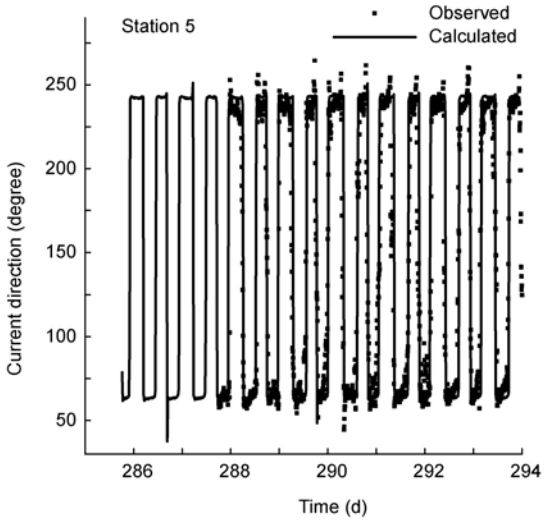

Figure 20 Measured and calculated current direction at Grays Harbor.

6 Conclusions

A depth-averaged two-dimensional tide and wave coupling model is presented for simulating flow phenomena of coastal waters in this study. Major characteristics and new idea of this coupling model include:

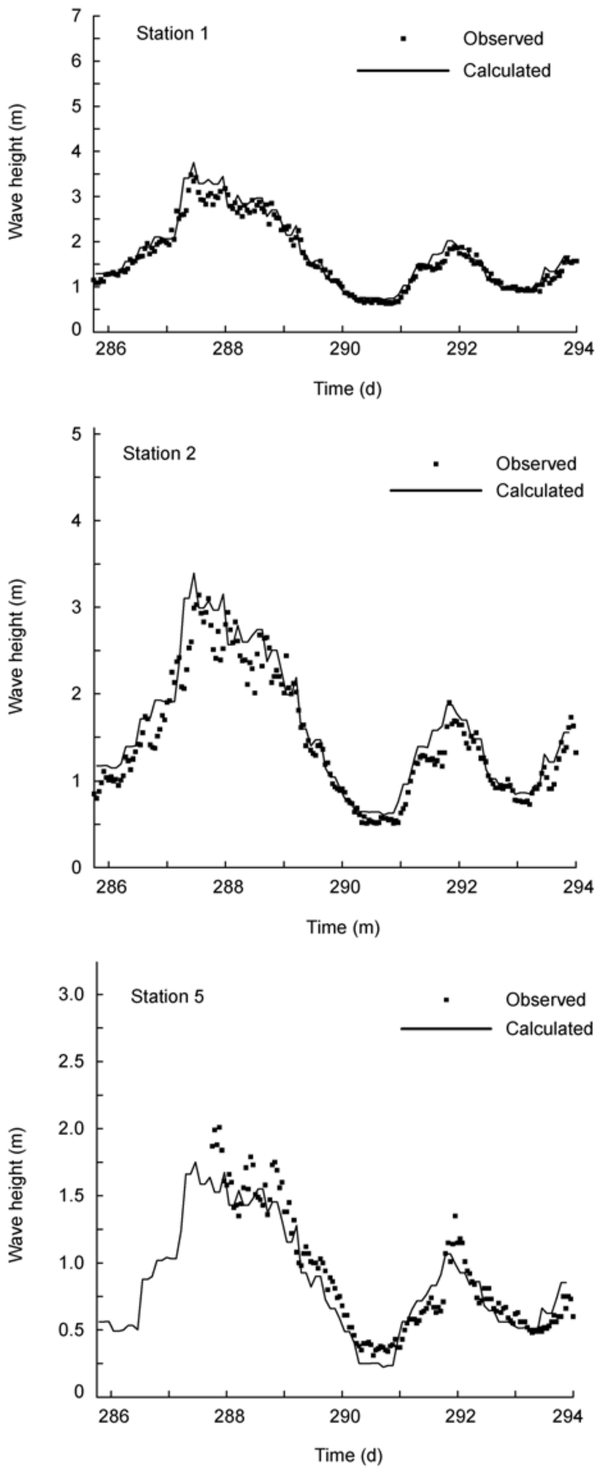

Figure 21 Measured and calculated wave heights at Grays Harbor.

1) This hydrodynamic model applies the non-staggered grid, all the primary variables are located at the center of cells, so the computer code is simpler and requires less memory, and the non-staggered grid is simpler in handling the interface between coarse and fine cells.

2) Such an unstructured model with quadtree mesh allows refining the grid for important computational domain, such as coastal inlet location, navigation channel.

3) The intercell fluxes are evaluated based on the HLL approximate Riemann solver with shock capturing property for capturing accurately the moving waterline and therefore, capable of simulating multiple flow regimes, in which subcritical, transcritical or supercritical flows may happen in the coastal waters.

4) The spectral wave action model can simulate wave fields by accounting for wave breaking, shoaling, refraction, diffraction, wind effect and current effect in coastal zones. Four parameterized wave breaking formulations are included in order to calculate accurately energy dissipation rate in the wave model under different conditions.

5) Dynamic coupling of the two models requires exchange of the information in an iterative process, the wave model needs to provide the results of radiation stresses, wave height and wave period for the hydrodynamic model. Meanwhile, the hydrodynamic model needs to provide the water level and velocity for the wave model.

The calculated results show good performance of the coupling model in predicting dam break flows, the unsteady tidal flow in estuaries and the longshore current generated by waves. These results show that the developed model is expected to be a useful tool for the study of many coastal phenomena in the future.

This work was supported by the National Natural Science Foundation of China (Grant No. 50839001), the research grant from Southeast Regional Research Initiative (SERRI, 80037) and the Coastal Inlets Research Program, ERDC, US Army Corps of Engineers, Vicksburg, MS, USA.

1 Magnus L, Nicholas C K. NMLONG: Numerical Model for Simulating Longshore Current. Technical Report 2, U.S. Army Corps of Engineer, Washington, DC, 2002
2 Wang T, Li J C. On wave-current interaction (in Chinese). Adv Mech, 1999, 29(3): 331–343
3 Duc B M, Wenka T, Rodi W. Numerical modeling of bed deformation in laboratory channels. J Hydraul Eng, 2004, 130(9): 894–904
4 Bradford S F, Sanders B F. Finite-volume model for shallow-water flooding of arbitrary topography. J Hydraul Eng, 2002, 128(3): 289–298
5 Yoon T H, Kang S K. Finite volume model for two-dimensional shallow water flows on unstructured grids. J Hydraul Eng, 2004, 130(7): 678–688
6 Begnudelli L, Sanders B F. Conservative wetting and drying methodology for quadrilateral grid finite-volume models. J Hydraul Eng, 2007, 133(3): 312–322
7 Wang G Q, Liu F, Fu X D, et al. Simulation of dam break development for emergency treatment of the Tangjiashan Quake Lake in China. Sci China Ser E-Tech Sci, 2008, 51(2): 82–94
8 Ying X Y, Jorgeson J, Wang S S Y. Modeling dam-break flows using finite volume method on unstructured grid. Eng Appl Comput Fluid Mech, 2009, 3(2): 184–194
9 Liang Q, Marche F. Numerical resolution of well-balanced shallow water equations with complex source terms. Adv. Water Resour, 2009, 32: 873–884
10 Valiani A, Caleffi V, Zanni A. Case Study: Malpasset dam-break simulation using a two-dimensional finite volume method. J Hydraul Eng, 2002, 128(5): 460–472
11 Xia J Q, Lin B L, Falconer R A, et al. Modelling dam-break flows over mobile beds using a 2D coupled approach. Adv Water Resour, 2010, 33: 171–183
12 Delis A I, Skeels C P. TVD schemes for open channel flow. Int J Numer Meth Fluids, 1998, 26: 791–809
13 Wang J S, He Y S, Ni H G. Two-dimensional free surface flow in branch channels by a finite-volume TVD scheme. Adv Water Resour, 2003, 26: 623–633
14 Liang D F, Falconer R A, Lin B. Comparison between TVD-MacCormack and ADI-type solvers of the shallow water equations. Adv Water Resour, 2006, 29 (12): 1833–1845
15 Brufau P, Garcia-Navarro, P. Two-dimensional dam break flow simulation. Int J Numer Meth Fluids, 2000, 33: 35–57
16 Rogers B D, Borthwick A G L, Taylor P H. Mathematical balancing of flux gradient and source terms prior to using Roe's approximate Riemann solver. J Comput Physics, 2003, 192: 422–451
17 Toro E F. Shock-Capturing Methods for Free-Surface Shallow Flows. England: Wiley, 2001
18 Kang L, Lee C H. A non-flux-splitting WENO scheme with low numerical dissipation. Sci China Tech Sci, 2010, 53: 3365–3378
19 Kuiry S N, Ding Y, Wang S S Y. Modelling coastal barrier breaching flows with well-balanced shock-capturing technique. Comput Fluids, 2010, 39: 2051–2068
20 Buttolph A M, Reed C W, Kraus N C, et al. Two-dimensional depth-averaged circulation model CMS-M2D: Version 3.0, Report 2. Sediment Transport and Morphology Change. Coastal Inlets Research Program. U.S. Army Corps Engineering, 2006
21 Tong F F, Shen Y M, Cui L. Numerical simulation of nearshore waves and wave-induced currents based on mild-slope equation in curvilinear coordinates (in Chinese). Sci Sin Phys Mech Astron, 2011, 41: 161–169
22 Wang J H, Shen Y M. Development and validation of a three-dimensional, wave-current coupled model on unstructured meshes. Sci Sin Phys Mech Astron, 2011, 54: 42–58
23 Park K Y, Borthwick A G L. Quadtree grid numerical model of nearshore wave–current interaction. Coast Eng, 2001, 42: 219–239
24 Greaves D. A quadtree adaptive method for simulating fluid flows with moving interfaces. J Comput Phys, 2004, 194(1): 35–56
25 Mase H. Multidirectional random wave transformation model based on energy balance equation. Coast Eng, 2001, 43 (4): 317–337
26 Zheng J H, Thanh N V, Zhang C. Spectral wave transformation model for simulating refraction-diffraction with strongly reflection coastal structure. Acta Oceanol Sin, 2011, 30(2): 25–32
27 Zheng J H, Mase H, Demirbilek Z, et al. Implementation and evaluation of alternative wave breaking formulas in a coastal spectral wave model. Ocean Eng, 2008, 35: 1090–1101
28 Nishimura H. Computation of neasrshore current. In: Horikawa K, ed. Nearshore Dynamics and Coastal Processes. Tokyo: University of Tokyo Press, 1988. 271–291
29 Wu W M, Sanchez A, Zhang M L. An implicit 2-D shallow water flow model on unstructured quadtree rectangular mesh. J Coastal Res, 2011, S1-59: 15–26
30 Kuriyama Y, Ozaki Y. Longshore current distribution on a bar-trough beach, Field measurements at HORF and numerical model. Report of Port and Harbour Research Institute 32(3), Ministry of Transport, Japan, 1993. 3–37
31 Li Z H, Nguyen K D, Brun-Cottan J C,et al. Numerical simulation of the turbidity maximum transport in the Gironde Estuary (in French). Oceanol Acta, 1994, 17(5): 479–500
32 Osborne P D, Hericks D B, Kraus N C, et al. Wide-area measurements of sediment transport at a large inlet, Grays Harbor, Washington. Proc 28th Int Conf on Coastal Engineering. Cardiff, UK: World Scientific, 2002. 1–13